ACS OMEGA

Open Access

http://pubs.acs.org/journal/acsodf

Article

Laser Melting of Mechanically Alloyed FeNi: A Study of the Correlation between Microstructure and Texture with Magnetic and Physical Properties

Shuvam Mandal, Manoj Kumar, Pradyut Sengupta, Ajit Panigrahi, Mayadhar Debata, Chandradas Shamili, Kuzhichalil Peethambharan Surendran, Indranil Manna, and Suddhasatwa Basu*

Cite This: *ACS Omega* 2024, 9, 15650−15662

Read Online

ACCESS | Metrics & More | Article Recommendations

ABSTRACT: The current study attempts to establish the interrelation between microstructure and magnetic properties induced during laser melting of the FeNi alloy. This study demonstrates the optimization of laser parameters for defect-free, uniform, and chemically homogeneous FeNi alloy synthesis. Mechanically alloyed FeNi (50−50 atom %) powders obtained after 12 and 24 h milling, with average particle sizes of 15 and 7 μm, were used as starting materials. It was found that the optimum range of laser power density for synthesis of dense and defect-free solids is between 1 and 1.4 J/mm^2. For laser melting under similar conditions, 12 h milled FeNi powder produces a larger grain (∼100 μm) with a preferred texture of (001), compared to 25 μm grain size in 24 h milled FeNi, with random texture. Smaller grain size is correlated with higher resistance to domain wall movement, resulting in higher coercivity and remanence in the laser-melted samples prepared from 24 h of milled powder. The presence of microtexture in laser-melted samples prepared from 12 h milled powder is related to a higher anisotropy.

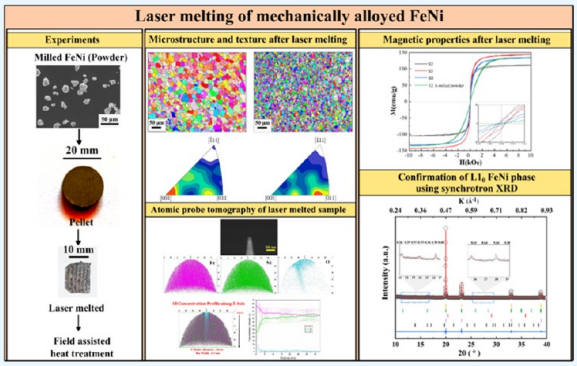

1. INTRODUCTION

Additive manufacturing of magnetic materials has kindled the interest of the research world due to the versatility of mechanical and metallurgical properties achieved by this process.[1−3] The current work focuses on FeNi alloys, which are extensively used in sensors, transformers, inductive devices, electric motors, etc., due to their good combination of soft magnetic properties and mechanical and electrical characteristics.[1−6] However, achieving the desirable magnetic properties along with mechanical strength is challenging.[1,2] Laser-based additive manufacturing provides an extremely versatile route for production of complex solid structures with the scope of controlling the microstructure by tuning the laser melting parameters. Laser melting provides extreme heating and solidification rates (∼10^6 K/s), which also facilitates formation of metastable phases.

This study primarily focuses on equiatomic FeNi, which is predominantly soft magnetic; however, it is also known to present hard magnetic properties in chemically ordered L1$_0$ form.[7−10] L1$_0$ FeNi is naturally found in meteorites and shows a high theoretical value of magnetic anisotropic constant (K_u = 1.35 MJ/m^3) owing to its ordered structure. The large K_u and high magnetic saturation (M_s = 1.47 T) produce a substantially high theoretical $(BH)_{max}$ value of ∼430 kJ/m^3.[10] Nonetheless, the artificial synthesis of this material on the bulk scale is not yet achieved.[10] The prime obstruction for the artificial synthesis of L1$_0$ FeNi is its instability above the order−disorder temperature (593 K).[10,11] Researchers have tried to achieve formation of L1$_0$ ordered FeNi by various non-equilibrium processing techniques at low temperatures.[12−18] Although these recent studies show the feasibility of laboratory synthesis of the L1$_0$ FeNi phase, it is worth mentioning that most of the experiments are done in powder form and no available literature shows clear evidence of the artificial formation of L1$_0$ FeNi in bulk materials.

Production of magnetic materials using laser melting is relatively new, and there are several variables, which need to be controlled, monitored, and optimized. Understanding and optimizing these parameters are still in the budding state. The literature on laser melting of FeNi alloys is primarily focused on the soft magnetic properties.[1,2,19] Chaudhary et al.[1] highlighted that laser melting of FeNi alloy produces a higher

Received: January 18, 2024
Revised: March 4, 2024
Accepted: March 6, 2024
Published: March 20, 2024

coercivity value, which is undesirable in the case of soft magnetic materials. However, increased coercivity is desirable for the current study on the hard magnetic property of FeNi.

The present work studies the microstructures and magnetic properties of the $Fe_{50}Ni_{50}$ alloy synthesized by laser melting. For the first time, the effect of laser processing on the interrelation between microstructural and magnetic properties is demonstrated. Heat treatment of laser-melted samples for an extended duration of 1000 h in the absence of a magnetic field and for 4 h in the presence of an external magnetic field is opted at T_{od}. The combined effect of laser melting and heat treatment is evaluated for the formation of $L1_0$ ordering in FeNi.

2. MATERIALS AND METHODS

2.1. Processing of FeNi Samples. FeNi alloys used for laser-based manufacturing were prepared from nickel (3−7 μm, Alfa Aesar, >99.9%, metals basis) and iron (<10 μm, Sigma-Aldrich, >99%, metals basis) powders. The Fe and Ni powders were mixed in an atomic ratio of 1:1 and mechanically alloyed using a dual-drive planetary ball mill. Our recent study has reported detailed work on the mechanical alloying of FeNi (50−50 atom %) alloy.[20] Mechanically alloyed FeNi powder was mixed with camphor (Sigma-Aldrich, purity 96%) to make pellets of 15 mm diameter and ∼4 mm height at an applied pressure of ∼270 MPa for 5 min, using a uniaxial press (Kimaya Engineers, India). Before laser melting, the pellets were heated in a debinding furnace (Nano tec, India) at 473 K to remove the binder. After debinding, pellets were melted using a 6 kW diode laser system (Laserline, Germany) integrated with a Kuka robotic system under an inert argon atmosphere.

The input power density is defined as

$$E_v = \frac{P}{v.\ h} \tag{1}$$

where P represents the input laser power, v is the scan speed, and h is the spot size (3.6 mm). The laser beam was scanned on the surface of the disk-shaped samples. Overlapping between the tracks was kept constant at 1.5 mm (∼41%) throughout the experiment for all of the specimens. Argon gas was filled continuously at 3 L/min to maintain a localized inert atmosphere. Table 1 summarizes the laser parameters and power density used for melting the samples.

Table 1. Parameters Used for Laser Melting of the FeNi Samples

laser power, P (W)	scan speed, v (m/s)	power density, E_v (J/mm^2)	nomenclature of samples: 12 h milled powder	nomenclature of samples: 24 h milled powder
500	0.1	1.4	S1	R1
	0.2	0.7	S2	R2
	0.3	0.4	S3	R3
750	0.1	2.0	S4	R4
	0.2	1.0	S5	R5
	0.3	0.7	S6	R6
1000	0.1	2.8	S7	R7
	0.2	1.4	S8	R8
	0.3	0.9	S9	R9

The laser-treated samples were heat treated just below 593 K for 1000 h using a quartz tubular furnace (Nano Tec., India) under vacuum conditions. Post 1000 h, the samples were transferred to a magnetic field-assisted furnace (Marine India, India). Further heat treatment for 4 h under an applied magnetic field of 1.5 T was carried out in an argon atmosphere. Details of the furnace are reported in ref 20.[20] Finally, the samples were quenched with argon at ∼40 °C/min to room temperature under a magnetic field.

2.2. Characterization of FeNi Samples. The surface of the laser-melted samples was cleaned using ultrasonication for 30 min. For the X-ray diffraction (XRD) study, samples were polished with 1500 and 2000 grit SiC abrasive papers. The polished samples were cut into uniform rectangular sizes for magnetic characterization with a 10 mm^2 (2 mm × 5 mm) area. For metallography, texture analysis, and nanoindentation, the laser-treated samples were polished using 800, 1000, 1500, and 2000 grit SiC abrasive papers and then fine polished for mirror finishing using microfiber cloth and diamond paste (∼1 μm), alumina suspension, and colloidal silica. Subsequently, the samples were etched using Adler's reagent to visualize grains. The microstructures of the FeNi samples were visualized using a field emission scanning electron microscope (FESEM) JEOL, JSM IT 800 SHL (Japan), operating at an accelerated voltage of 30 kV. Compositional analysis was conducted using energy-dispersive X-ray spectroscopy (EDS) coupled with FESEM. Electron backscatter diffraction (EBSD) analysis was performed to generate inverse pole figure (IPF) maps and to quantify crystallographic orientations using a high-velocity detector (EDAX). The step size for the EBSD measurement was 0.2 μm. The EBSD data were collected on the surface and along the cross-section of the sample at a distance of 1 mm from the edge and analyzed using the MATLAB texture (MTEX) toolbox.[21−23] Atomic probe tomography (APT) experiments were conducted using a Cameca Local Electrode Atom Probe (LEAP) 5000XR instrument with a laser wavelength of 355 nm (UV) at the National Facility for Atom Probe Tomography (NFAPT), IIT Madras, Chennai, India. Needle-shaped specimens for APT analysis were extracted using an FEI Nova 200 dual-beam focused ion beam (FIB) instrument. XRD analysis was conducted with Cu Kα radiation, operated at 30 kV using a Rigaku diffractometer. Synchrotron XRD (SXRD) measurements of laser-melted FeNi samples were performed at Indus-2, the Indian synchrotron radiation source, using the ADXRD beamline (BL-12). The measurements used six circle diffractometers (Huber 5020) with a one-dimensional (1D) position-sensitive detector (Mythen). A high-energy X-ray beam with an energy of E = 17.17 keV (λ = 0.7231 Å) was directed at the FeNi samples. Variations of magnetization with respect to the applied magnetic field and temperature of FeNi laser-melted samples were investigated by using a vibrating sample magnetometer attachment to a Physical Property Measurement System (Quantum Design, DynaCool). The magnetic properties of the laser-melted samples were measured parallel to the solidification direction (SD). The high-temperature magnetic measurements in the temperature range of 400−800 K were carried out using a VSM-oven attachment.

3. RESULTS AND DISCUSSION

3.1. Analysis of Mechanically Alloyed FeNi Powders. Figure 1 shows the particle size distributions for 12 and 24 h of

https://doi.org/10.1021/acsomega.4c00601
ACS Omega 2024, 9, 15650−15662

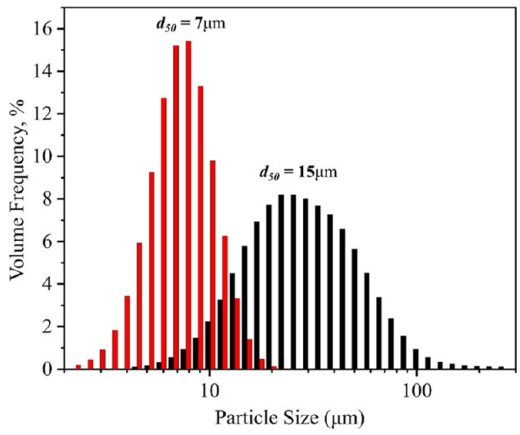

Figure 1. Particle size analysis showing the frequency distribution of particles for 12 h milled (black) and 24 h milled (red) FeNi powders.

milled FeNi powders. It is noticed that with increased milling duration the particle size distribution becomes narrow and the median particle size (d_{50}) decreases from 15 to 7 μm.

3.2. Effect of Laser Melting on Microstructure. Figure 2a,b shows the comparison of melt pool thickness with respect

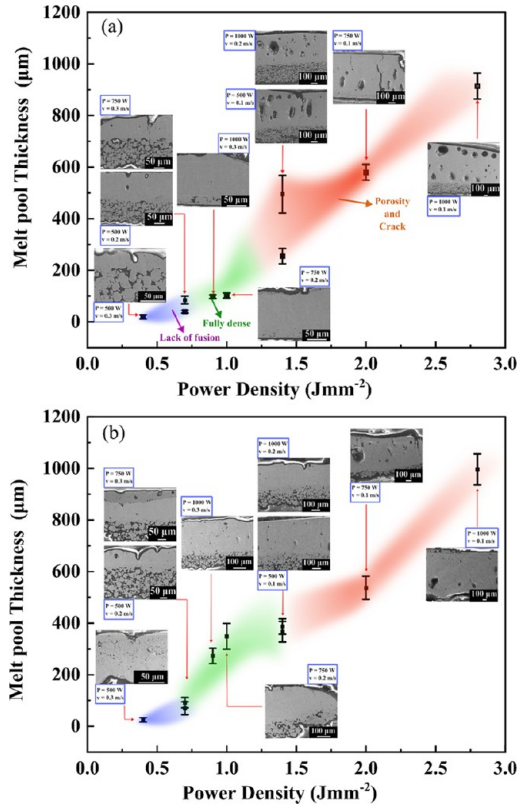

Figure 2. Correlation of laser power density and microstructure of the cross-section of melt pool prepared from (a) 12 h milled and (b) 24 h milled FeNi powders.

to the laser power density for samples prepared from 12 to 24 h milled powder, respectively. From Figure 2a,b, it is evident that samples prepared using power density ≤0.7 J/mm^2 have defects arising due to lack of proper fusion during laser melting (shown by the blue region). Samples prepared under laser power densities of 1 and 1.4 J/mm^2 resulted in defect-free continuous melted samples (shown by the green region). Samples prepared with power density >1.4 J/mm^2 show blow holes and microcracks (shown by the red region). Spherical pores are noticed at higher power densities, which can be attributed to rapid changes in the melt pool shape and surface vaporization. Studies on laser melting parameter optimization for high silicon steel[24] and FeNi[25] show similar defect profiles at higher power densities. Also, these studies found that the working range of power density for Ni-based materials to synthesize defect-free solids was 1.5 to 2 J/mm^2 for a starting particle size of 40−80 μm.[25,26] It is noticed that the green zone is broader for 24 h milled powder compared to that of 12 h milled powder (Figure 2a,b). Comparing the melt pool thickness, it is clear that the laser melting of 24 h milled powder produces a larger melt pool compared to 12 h milled powder. This may be attributed to the decrease in particle size and increase in uniformity of powder particles after 24 h milling. The effect of initial particle size on the laser-melting microstructure of iron[27] and tungsten[28] was well studied. It was found that decreasing particle size increases the melt pool size due to the availability of a large surface area, facilitating the absorbance of laser energy. Also, it is observed that the inhomogeneity in particle shape and size causes a decrease in melt pool size due to a lower heat transfer rate.[27−30] The current work examined the density of the green pellets used for laser melting experiments. It was found that pellets made from 12 h of milled powder had a density of 60 ± 2% of the theoretical density, whereas pellets made from 24 h of milled FeNi had a density of 67 ± 3%. The above observation is also backed by the surface of the green pellets, which show better packing in the 24 h milled powder. The density of the green pellet plays an important role in the formation of the melt pool. The average pore fraction for 24 h milled green pellets is ∼7% less than that for 24 h milled pellets. Hence, heat conduction is favorable in the 24 h milled powder pellets. The combined effect of a smaller particle size and a higher rate of conduction in the 24 h milled pellets led to a higher melt pool thickness in these samples.

Figure 3a−c shows the microstructure of the surface of laser-melted samples S2, S5, and S8 (power densities of 0.7, 1, and 1.4 J/mm^2) prepared from 12 h of milled FeNi alloy powders. It can be observed that the average grain size varies from 20 to 30 μm for S2 to ∼50−70 μm for S5 and >100 μm for S8. Also, the pores on the laser-melted surface are fewer. Only a few spherical pores of <10 μm are visible. Figure 3d−f shows the microstructure of the surface of laser-melted 24 h milled FeNi powder (R2, R5, and R8). It can be observed that the grain size for R2 and R5 melted samples is comparatively similar (15−30 μm), whereas, for the R8 melted sample, the grain size is ∼100 μm. Comparing the cross-sectional microstructures in Figure 2, it can be inferred that power densities of 1 and 1.4 J/mm^2 are most suitable for laser melting of FeNi milled powders. Also, from Figure 3, it can be concluded that grain size enhancement is positively correlated with an increased laser power density. As the extrinsic magnetic properties are known to depend on the grain size, in this work, further characterization is carried out for the laser-melted defect-free samples with moderate grain sizes, prepared at a power density of 1 J/mm^2 (i.e., S5 and R5).

Figure 4 shows the compositional profiles of the laser-melted FeNi samples prepared from 12 to 24 h milled powders (S5 and R5) along the cross-section. It is evident that the composition of the laser-melted samples is uniform. The composition for sample S5 is 51.6 ± 3.5 atom % Fe and 48.4 ±

https://doi.org/10.1021/acsomega.4c00601
ACS Omega 2024, 9, 15650−15662

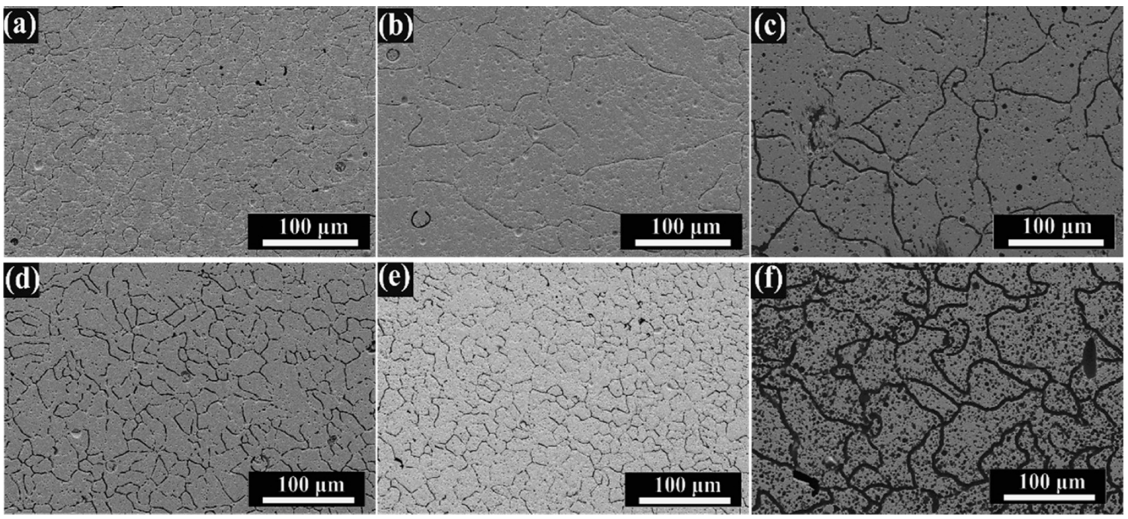

Figure 3. SEM of the etched surface of laser-melted 12 h milled powder (a) 0.7 J/mm^2, (b) 1 J/mm^2, and (c) 1.5 J/mm^2: SEM of the etched surface of laser-melted 24 h milled powder, (d) 0.7 J/mm^2, (e) 1 J/mm^2, and (f) 1.5 J/mm^2.

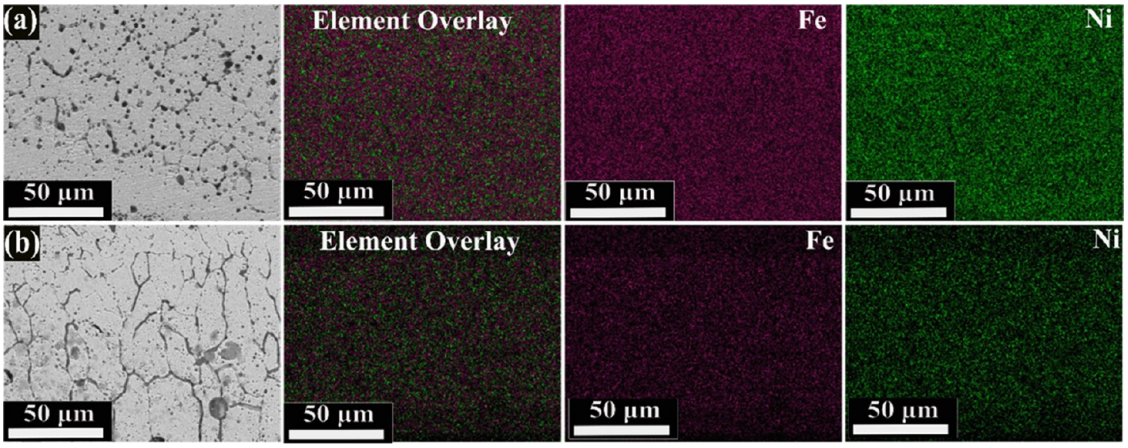

Figure 4. Elemental map showing the distribution of Fe and Ni in the bulk sample of 750W 0.2 m/s laser-melted (a) 12 h and (b) 24 h milled FeNi alloy.

3.2 atom % Ni, and for sample R5, the composition is 49.9 ± 3.7 atom % Fe and 50.1 ± 3.8 atom % Ni. To further investigate how Fe and Ni atoms are distributed in the solid solution and whether there is any short-range ordering formed due to laser melting, APT studies were conducted on R5. Compared to SEM (EDS) or even transmission electron microscopy (TEM) (EDS), APT provides three-dimensional (3D) chemical information on the material on a near-atomic scale. Here, Figure 5a shows the 3D elemental maps, confirming the atomic distribution in R5. It shows that there is no apparent segregation of alloying elements present in the as-melted sample. Figure 5b shows 1D concentration profiles along a cylindrical region with a diameter of 10 nm and a fixed bin size of 0.5 nm. It can be observed that the concentration of Fe and Ni deviated significantly from the ideal 50−50 atom % and a small amount of oxygen is present up to a depth of 2.5 nm. The formation of oxides is also evident in Figure 5a, which shows the presence of oxygen at the top of the sample subjected to APT. At this point, it should be mentioned that although present the amount of oxide is extremely low, as detected by the APT analysis. Bulk analyses like XRD and SEM (EDS) show no evidence of oxygen contamination. Therefore, the oxygen content is expected to be in a lower quantity and form a small amount of $NiFe_2O_4$ during sample preparation or handling. $L1_0$ ordered FeNi could not be detected by using the APT technique. The inability of APT to detect short-range ordering in FeNi is attributed to the statistical errors associated with the low cross-sectional dimensions of the measurement bar and the low bin size. The statistical error is defined as $E = \sqrt{\frac{c_i(1-c_i)}{N}}$, where c_i is the concentration of element ith, and N is the number of atoms. It is clear that with the cross-section of the measuring cylinder and the bin size being 10 and 0.5 nm, the error is quite substantial to hinder the detection of short-range ordering.[31]

The Young's modulus and nanohardness of laser-melted samples (S5 and R5) were evaluated using a nanoindentation setup (Bruker Hysitron) at a load of 5 mN. The nanohardness value for samples S5 and R5 is 4.58 and 4.55 GPa, respectively. These hardness values are comparable with that of the tetrataenite phase of the Taza meteorite.[32]

3.3. Texture in Laser-Melted FeNi. Figure 6a,b shows the inverse pole figure (IPF) maps of S5 and R5, respectively. The first notable difference between the two images is the grain size. Sample S5 shows relatively larger grains (~100 μm) than R5 (~25 μm). Also, equiaxed grains are observed in both S5

https://doi.org/10.1021/acsomega.4c00601
ACS Omega 2024, 9, 15650−15662

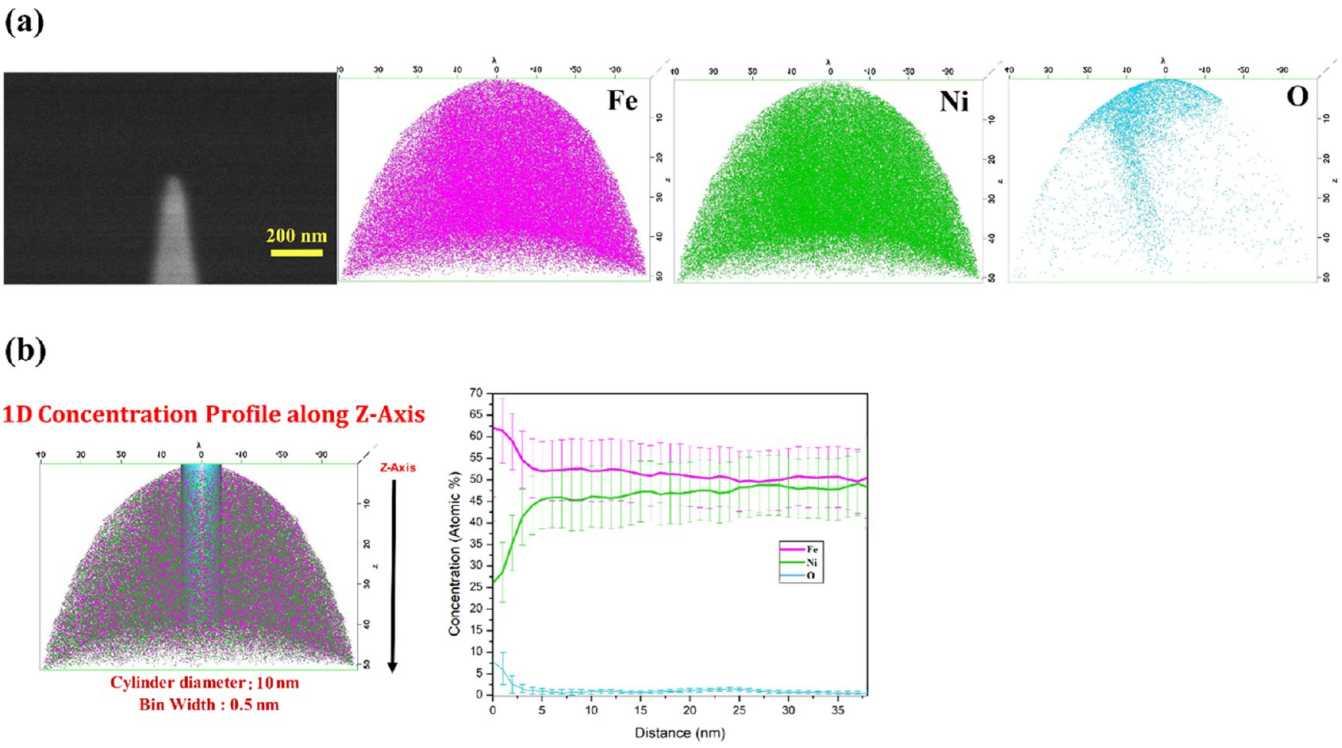

Figure 5. Atomic probe tomography image: (a) elemental map showing the distribution of Fe and Ni and (b) elemental analysis with respect to the depth of the sample.

and R5. The smaller grain size in R5 compared to S5 can be explained by the smaller particle size of the initial powder before laser melting operation and the higher green density of R5, resulting in higher energy absorption because of the higher surface area to volume ratio. This leads to the formation of higher melt pool thickness in R5. Upon cooling, it solidifies faster, resulting in a smaller grain size in R5. Figure 6c,d shows the IPF maps of the cross-section of S5 and R5, respectively. Here the solidification direction (SD) is indicated toward the left ($-X$ direction). Columnar grains are noticed along the SD, which is expected as grains grow preferentially along the solidification direction upon cooling the melt pool; i.e., a higher fraction of elongated grains is observed at the surface than away from the surface. Similar columnar grains are observed along the build direction for selective laser melting of Ni-based alloys.[26,33−35] In the IPF maps, the black regions are unindexed points that refer to pores present in the sample. Figure 6e,f shows the IPFs for S5 and R5 of the IPF maps presented in Figure 6c,d, respectively. IPFs are constructed for the crystal orientation along the solidification direction. In the case of S5, the grains are oriented with a strong <001> texture along SD, whereas, in the case of R5, the <034> crystallographic direction becomes dominant along SD. The easy axis of magnetization for FeNi alloy is along the <001> direction,[36] and it is evident from the IPF (Figure 6c) that the easy axis is oriented perpendicular to the solidification direction for S5. Strong <001> texture is common for laser-melted Ni-based alloys,[34] which shows that the crystal growth is parallel to the solidification direction. However, in the case of R5, the easy axis of magnetization is not aligned along the solidification direction. Interestingly, it is reported that when the crystal growth is not parallel to the build direction, a weak <011> texture is also possible.[33,34] The smaller starting particle size may have induced extremely rapid cooling rates during solidification, which did not allow the formation of <001> texture in the R5 sample.

3.4. Phase Analysis. The XRD patterns of the starting powders and the subsequent laser-melted samples are presented in Figures 7 and 8, respectively. Figure 7a compares the XRD patterns of the laser-melted S2, S5, and S8 with 12 h of milled powder. Similarly, Figure 8a compares the 24 h milled FeNi powder with the corresponding R2, R5, and R8. Figures 7b and 8b show the standard patterns of face-centered cubic (FCC) FeNi and $L1_0$ FeNi. It can be observed that all of the fundamental peaks of both FCC and $L1_0$ FeNi coincide. Also, it may be noted that the superlattice peaks of $L1_0$ FeNi are extremely difficult to resolve using conventional XRD due to the small difference in X-ray scattering length for elemental Fe and Ni, making intensity ratios of the strongest superlattice peaks and fundamental peaks as small as 0.3%.[10] Figures 7c and 8c show the enlarged view of the XRD plot for the 2θ values of 20−40°, where the positions of $L1_0$ FeNi superlattice peaks are discernible. Although there is an indication of the presence of superlattice peaks for the S5, S8 (Figure 7c) and R2 and R5 (Figure 8c), it is extremely difficult to resolve them accurately from the background spectra. Furthermore, the (100) superlattice peak of $L1_0$ FeNi coincides with the (311) fundamental peak of $NiFe_2O_4$. Spontaneous formation of $NiFe_2O_4$ is possible during material handling and characterization.[14,20] Figures 7d and 8 d show XRD patterns in the range of 42−45° of Figures 7a and 8a, respectively. An increase in the intensity of the (111) fundamental peak from the powder form to the laser-melted samples is observed, which can be attributed to the increase in the crystallinity of the sample during recrystallization. Williamson Hall (W-H) plots were drawn using the following equation:

https://doi.org/10.1021/acsomega.4c00601
ACS Omega 2024, 9, 15650−15662

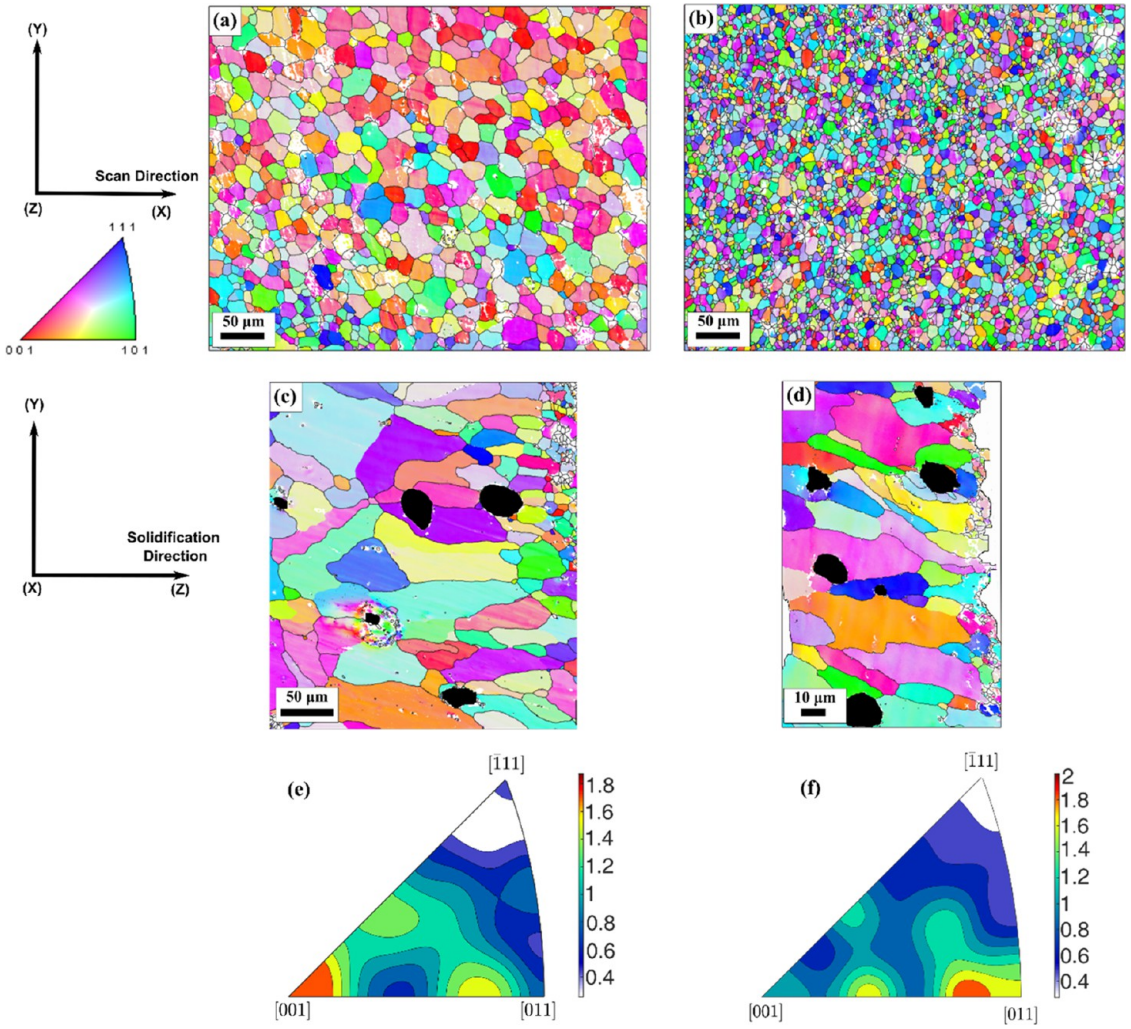

Figure 6. EBSD IPF images of the surface of (a) S5 and (b) R5 and cross sections of (c) S5 and (d) R5. (e) and (f) represent IPFs for the image in (c) and (d), respectively.

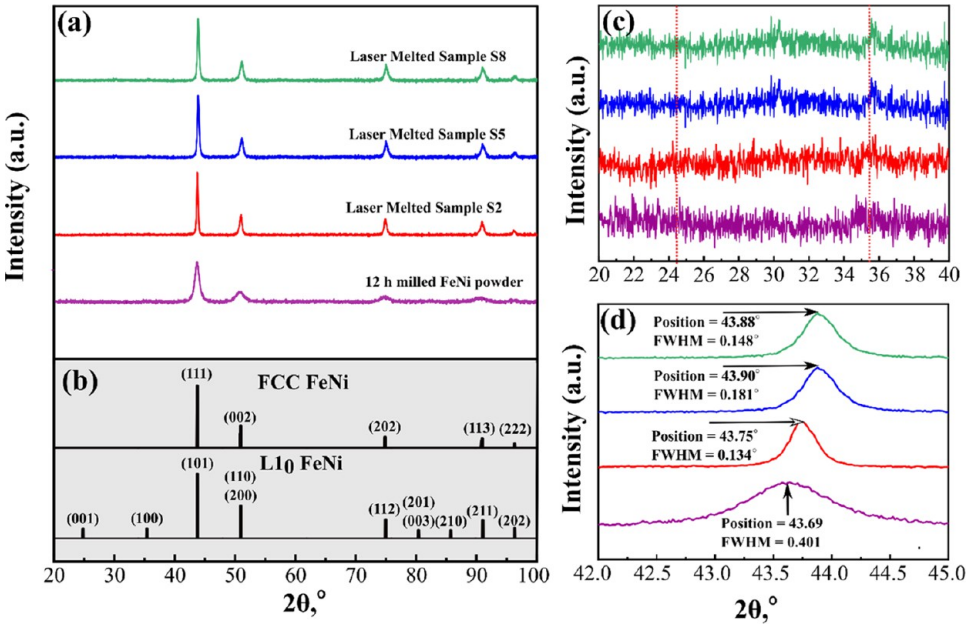

Figure 7. (a) Comparison of XRD of laser-melted FeNi prepared from 12 h milled FeNi powder. (b) Standard pattern for FCC and $L1_0$ FeNi. (c) XRD pattern from the 2θ position of 20−40°. (d) Image showing XRD pattern shift due to laser energy.

https://doi.org/10.1021/acsomega.4c00601
ACS Omega 2024, 9, 15650−15662

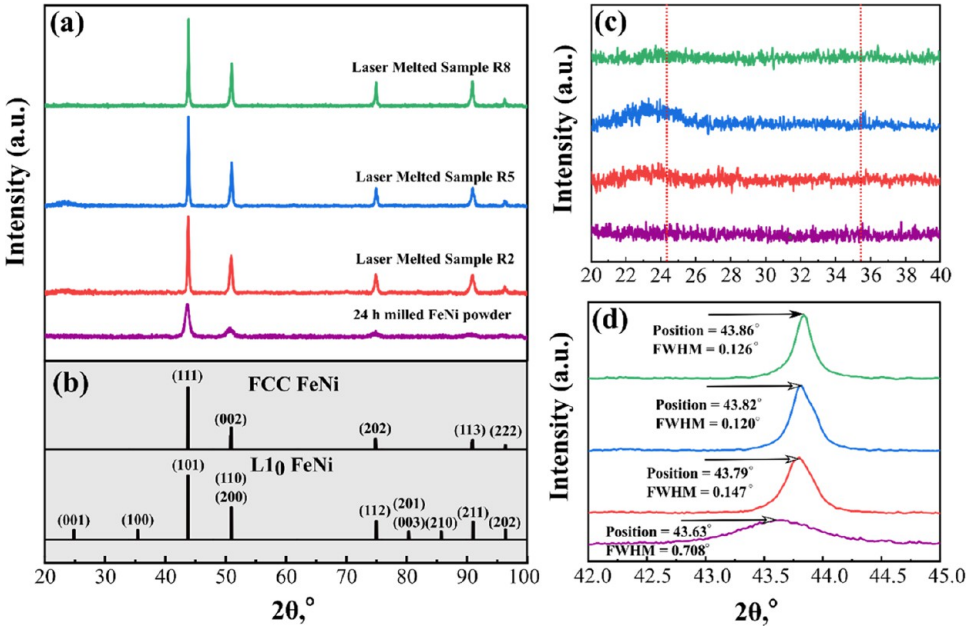

Figure 8. (a) Comparison of XRD of laser-melted FeNi prepared from 24 h milled FeNi powder. (b) Standard pattern for FCC and $L1_0$ FeNi. (c) XRD pattern from the 2θ position of 20−40°. (d) Image showing XRD pattern shift due to laser energy.

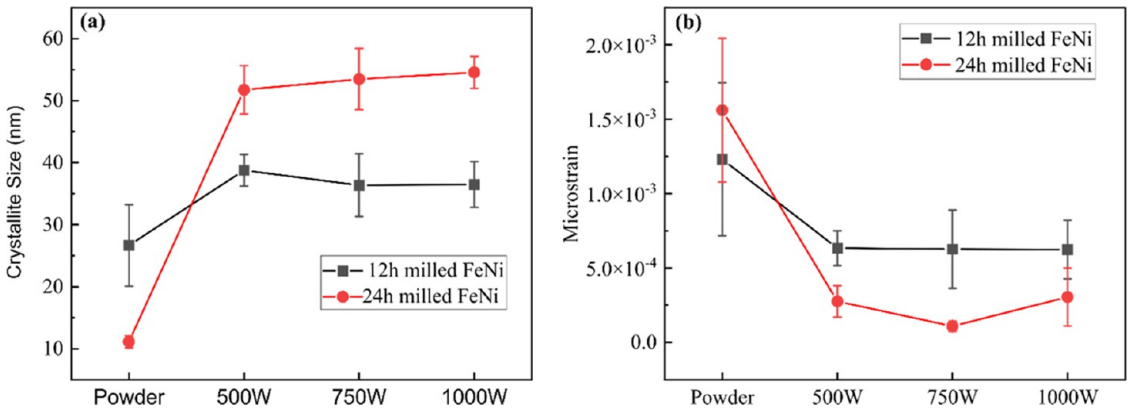

Figure 9. Comparison of (a) crystallite size and (b) microstrain calculated from W-H plots.

$$\beta_r \cos\theta = \frac{k\lambda}{t} + \eta \sin\theta \quad (2)$$

where λ is the wavelength of incident X-ray (in nm), k is a constant (usually 0.9−1), t is the crystallite size in nanometers, θ is Bragg's angle (in radian), and η is the strain induced in the material. β_r is the instrument-corrected full width at half-maximum (fwhm) of the diffraction peaks (in radians). From the W-H plots, strain and crystallite size were extracted from the slope and the intercept of the linear best-fit line. The comparison of crystallite size and microstrain is shown in Figure 9. It is noted that the crystallite size increases substantially with laser melting. In the case of 12 h milled FeNi, the crystallite size increases to ∼40 nm from ∼26 nm. However, with the increase in laser power, the crystallite size remains the same, considering the standard error in the measurement. For 24 h milled FeNi, the crystallite size increases to a larger value, i.e., from ∼10 nm in powder to ∼55 nm upon laser melting. Interestingly, the grain size of laser-melted 12 h milled FeNi powder, measured by EBSD, is ∼100 μm, whereas that of 24 h milled FeNi powder is found to be 25 μm. However, the trend of having lower grain sizes in laser-melted 24 h milled FeNi powder than in 12 h milled FeNi powder is not reflected in the crystallite size measurements from the W-H plots. The increase in crystallite size can be linked to the annihilation rate of the defects during the laser melting and subsequent cooling of the milled powders. Twenty-four hours milled FeNi powder possesses a higher concentration of defects than 12 h milled FeNi because of milling for a high duration. Thus, during instant melting by laser, it is expected that a large amount of defect annihilation takes place in the 24 h milled FeNi case, which forms larger defect-free zones in the grains upon cooling, reflected as crystallites. The microstrain measurements from the W-H plots also corroborate this finding. The microstrain in 24 h milled FeNi is lower than that of 12 h milled FeNi.

In an earlier study through SXRD analysis, we showed that 12 h milled FeNi powder contains ∼9 wt % $L1_0$ FeNi phase along with a 90 wt % FCC FeNi phase, a small amount of <1 wt % of unreacted Fe, Ni, and about <0.5 wt % of $NiFe_2O_4$.[20] Now, it is imperative to ascertain that a $L1_0$ phase exists in the laser-melted sample. Conventional XRD of the laser-melted sample indicates the possibility of $L1_0$ ordering due to the

https://doi.org/10.1021/acsomega.4c00601
ACS Omega 2024, 9, 15650−15662

presence of superlattice peaks in Figures 7c and 8c. However, the peak intensities are not sufficient enough to quantify the phase. It is very difficult to distinguish from the background noise. Therefore, in this study, SXRD investigation (λ = 0.7227 Å) was carried out for S5 to observe the superlattice peaks. The SXRD pattern of S5 is shown in Figure 10. This pattern

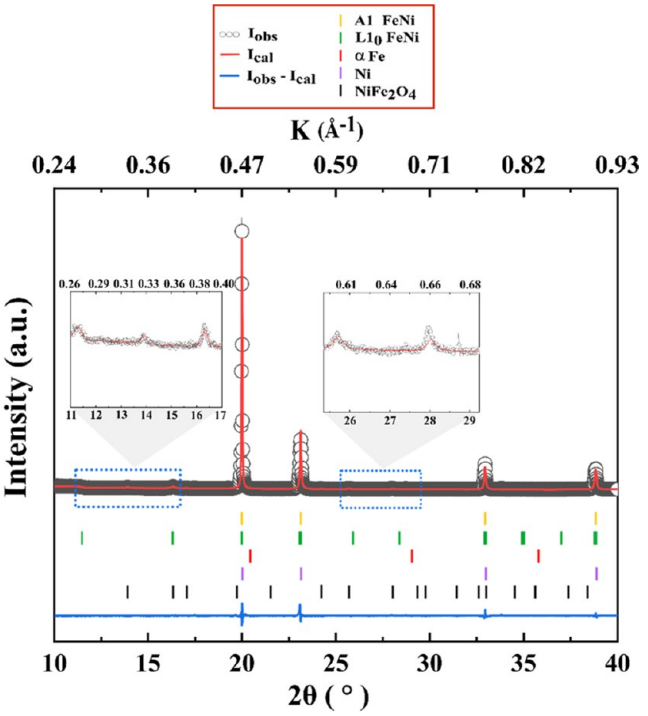

Figure 10. Rietveld refinement of the SXRD pattern of sample S5.

clearly shows the presence of (001), (100), (201), and (210) superlattice reflections, indicating the presence of $L1_0$ ordering. The quantification of the phases was done using Rietveld analysis with Fullprof software. The refinement parameter chi-squared value quantifies the quality of Rietveld refinements and is expressed as $\chi^2 = (R_{wp}/R_{exp})^2$, where R_{wp} and R_{exp} are the weighted profile R-factor and expected R-factor, respectively. The values of χ^2, R_{wp}, and R_{exp} are 6.66, 14.29, and 5.54, respectively. The difference between experimental and calculated intensities is presented below the pattern fit. The Rietveld analysis shows 86 wt % FCC FeNi, 9.5 wt % $L1_0$ FeNi, <2 wt % of unreacted Fe, <2 wt % Ni, and a trace amount of <0.5 wt % $NiFe_2O_4$. From this finding, it is concluded that $L1_0$ ordered FeNi is present after laser melting.

3.5. Magnetic Properties. *3.5.1. As-Laser-Melted Samples.* Figure 11a shows the hysteresis loops (M-H curves) for samples S2, S5, and S8, compared to the 12 h milled powder. It is observed that S5 has the highest saturation magnetization (M_s) of 144 emu/g, which is slightly higher than the value of 137 emu/g of 12 h milled powder. The M_s values for the samples S2 and S8 are ∼111 and 132 emu/g, respectively, which are around 28 and 14% less than the reported value of M_s for $L1_0$ FeNi (154 emu/g) in a single crystal.[15] M-H curves for R2, R5, and R8 compared to 24 h milled powder are shown in Figure 11b. Following the previous trend, R2 and R8 show a relatively lower value of M_s than R5. R5 shows an M_s value of 143.5 emu/g. It may also be noted that S2 and R2 show the minimum value for M_s in the respective batches. The lower M_s value of S2/R2 and S8/R8 compared to S5/R5 can be traced to porosity and macrodefects in the samples. As discussed in Section 3.2, the densification is lower in S2 or R2 samples due to the induction of relatively low power density during laser melting, causing porosity. Also, S2 and R2 have microscopic discontinuities in the melt pool. However, in samples S8 or R8, although the melt pool is continuous, pinhole defects and cracks are prevalent. These sample defects act as hotspots for oxygen pickup, facilitating oxide formation. The presence of a small amount of oxides leads to a significant decrease in M_s. It may be noted that the microscopic unmelted regions in S2/R2 provide a much diverse range of active sites for oxidation, thus resulting in the lowest saturation values. The above observation again validates that laser power 1 J/mm^2 is the most optimum condition for producing $L1_0$ ordered FeNi. The inset of Figure 11a,b shows the M_r and H_c values for the respective samples. In both cases, the H_c and M_r for the laser-melted samples are higher than those for the milled powders, which shows typical soft magnetic behavior with negligible M_r. The H_c values of samples S2, S5, and S8 are in the range of 20−30 Oe. The values of M_r for S2, S5, and S8 are in the range of 10−12 emu/g, which is 20 times higher than that of the powder samples. In the case of R2, R5, and R8, a similar trend

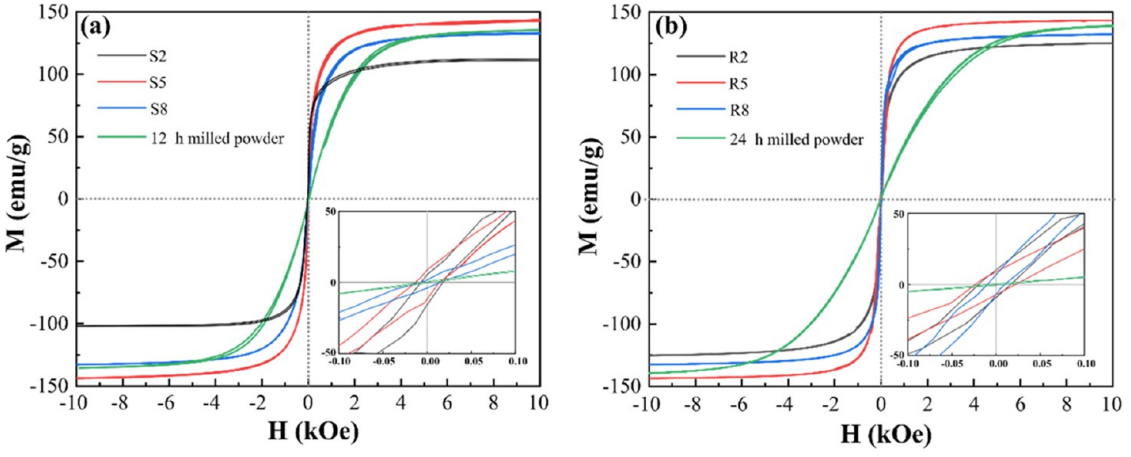

Figure 11. Hysteresis (M-H curves) for (a) 12 h milled FeNi powder, laser-melted S2, S5, and S8 and (b) 24 h milled powder, laser-melted R2, R5, and R8.

https://doi.org/10.1021/acsomega.4c00601
ACS Omega 2024, 9, 15650−15662

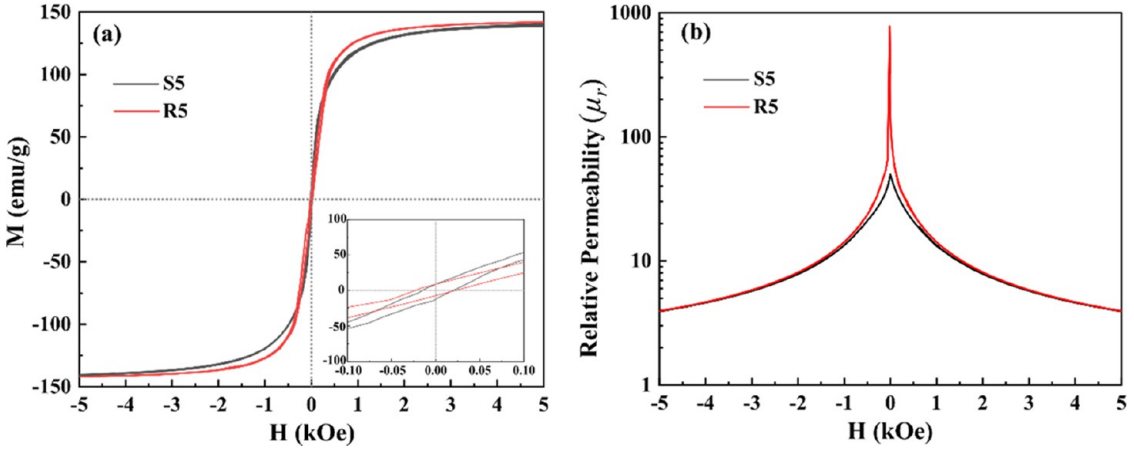

Figure 12. (a) M-H plot of sample S5 (black) and R5 (red) and (b) relative permeability vs H for S5 (black) and R5 (red).

Table 2. Comparison of Properties of $L1_0$ FeNi in the Literature

s. no.	processing technique	composition (atom %)	vol. % of $L1_0$ FeNi	long-range ordering parameter (s)	FeNi particles' shape and size	magnetic saturation (M_s) (emu/g)	hysteresis (H_c) Oe	ref
1	natural meteorite (NWA 6259)	44% Ni, 54% Fe, trace impurity of Co, Cu, P	95		1 μm thick ring along grain boundary of FCC FeNi	143.7	1000	39,40
2	neutron irradiation of the FeNi single crystal	50% Ni, 50% Fe		0.41−0.45				11,15
3	cyclic oxidation and reduction of Ni-coated Fe	50% Ni, 50% Fe	19					41
4	deposition of the monatomic layer of Fe and Ni using molecular beam epitaxy	50% Ni, 50% Fe		0.2−0.6		140−180	1000−1350	42−49
5	nitrogen insertion and topotactic extraction	50% Ni, 50% Fe	100	0.71	90 nm (powder)	144	1784.42	14
6	crystallization from amorphous FeNiSiBPCu bulk metallic glass	42% Fe, 41.3% Ni, 8% Si 4% B, 4% P and 0.7% Cu	8	0.8	30−50 nm sized polycrystalline grains	100	700	36,50
7	crystallization from amorphous FeNiPC bulk metallic glass	40% Fe, 40% Ni, 13% P and 7% C			<100 nm dispersed in bulk	82	641	13
8	high-pressure torsion of meteorite (Morasko Meteorite)	51% Fe and 49% Ni				108−150	30−80	38
9	high-pressure torsion of FeNi and heat treatment	50% Fe, 50% Ni	absent			144.7	3.8	51
10	laser melting of FeNi alloyed powder	50% Fe, 50% Ni	9.5			144	50	this work

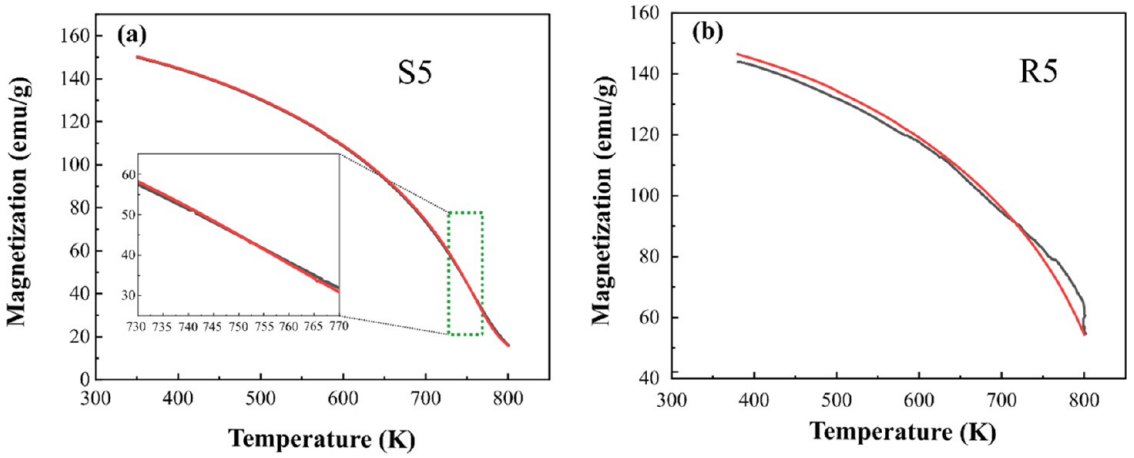

Figure 13. Magnetization vs temperature (M-T) for laser-melted (a) S5 and (b) R5.

is observed, where the H_c values are in the range of 40−50 Oe and the M_r values are in the range of 10−15 emu/g.

Figure 12a compares the M-H curves (hysteresis loops) of S5 and R5. H_c and M_r are extrinsic magnetic properties and

https://doi.org/10.1021/acsomega.4c00601
ACS Omega 2024, 9, 15650−15662

depend profoundly on density, microstructural features like grain size, pores, cracks, and structural defects. The grain boundaries and defects retard the movement and rotation of magnetic domains, causing an increase in coercivity.[37] The inset of Figure 12a compares coercivity (H_c) and remanence (M_r) between the peaks of S5 and R5. The H_c value of S5 was recorded at 20 ± 5 Oe and that of R5 was 50 ± 8 Oe. The higher H_c value for R5 could be attributed to the smaller grain size. A comparison of H_c of FeNi prepared by different processing techniques to that in the present work is summarized in Table 2. Most of the literature is dedicated to extremely small nanoparticles, which may lead to the formation of single domains of $L1_0$ FeNi, thus showing higher coercivity. The H_c value obtained in this work is comparable to that of severe plastic-deformed FeNi.[38]

Figure 12b compares the relative permeability ($\mu_r = B/H$) of S5 and R5 with respect to the applied magnetic field (H). It can be observed that μ_r increases from S5 to R5. Previous studies on laser-melted nickel alloys have highlighted that the presence of <111> or <110> texture causes relative permeability to increase.[25] On the other hand, the presence of <001> texture causes μ_r to decrease. The present work shows that S5 has a <001> fiber texture, while R5 shows an <430> orientation along SD. This finding is well aligned with the fact that S5 has lower permeability than R5. Therefore, the rate of magnetization for R5 is higher than that of S5.

Further, temperature-dependent magnetization measurements (M-T) of laser-melted FeNi samples were done. Figure 13 shows the magnetization vs temperature (M-T) graphs of laser-melted S5 and R5. The heating curve in Figure 13 is colored red, and the cooling curve is shown in black. It can be observed from Figure 13a,b that the cooling curve crosses the heating curve at 720 K. This could be due to the order-to-disorder transformation of the $L1_0$ phase present in the system. Although the reported value of the order−disorder temperature for $L1_0$ FeNi is around 593 K, many researchers highlight that the order−disorder process is kinetically limited and the actual temperature for disordering may vary depending on the heating rate. Bordeaux et al.[52] studied the thermodynamic and kinetic properties of $L1_0$ FeNi in meteorites using a differential scanning calorimeter (DSC). They found that the order−disorder transformation is detected in DSC as an endothermic peak at 798 K when the heating rate is 1 K/min and changes to 875 K when the heating rate is 25 K/min. This work presents a similar onset temperature of the order−disorder transformation at 720 K with a heating rate of 5 K/min.

3.5.2. After Heat Treatment of Laser-Melted Samples. It is reported by Bordeaux et al.[52] that the diffusion constant for FCC FeNi below the order−disorder temperature of 593 K is in the order of 10^{-27} cm^2/s. The value of the diffusion constant physically signifies that near the order−disorder temperature, a single atomic jump will take as long as 2600 years. It can be inferred that the formation of $L1_0$ ordering in FeNi is difficult using conventional heat treatment methods. Recent studies show that electric[53] and magnetic[54] field-assisted annealing at low temperatures may assist the formation of $L1_0$ ordering in FeNi. In this work, the heat treatment of S5 and R5 was carried out just below 593 K for 1000 h without applying a magnetic field. Additionally, these samples were further subjected to a 4 h heat treatment at the same isothermal temperature under a magnetic field of 1.5 T. Figure 14a compares the M-H curves of 1000 h heat treated (without an external field) and an additional 4 h heat-treated (with an external magnetic field) S5 samples. It is observed that the M_s value does not change with heat treatment. The inset image in Figure 14a shows that the H_c and M_r values are similar to those of the as-melted samples. The rate of magnetization is slightly higher in the case of the sample heat treated in the presence of an external magnetic field. This can be attributed to the alignment of the domain due to the applied field, which allows the sample to attain saturation at a comparatively lower field during VSM measurement. Figure 14b shows the effect of heat treatment (with and without applying a magnetic field) of the R5 sample on B−H curves. Similar findings to that of sample S5 are observed. It is clear from the above result that there is no profound effect of heat treatment near the order−disorder temperature in solid FeNi. Applying a magnetic field during heat treatment also does not have an observable difference in the magnetic properties of the FeNi samples, indicating no change in the $L1_0$ phase concentration in the bulk during heat treatment.

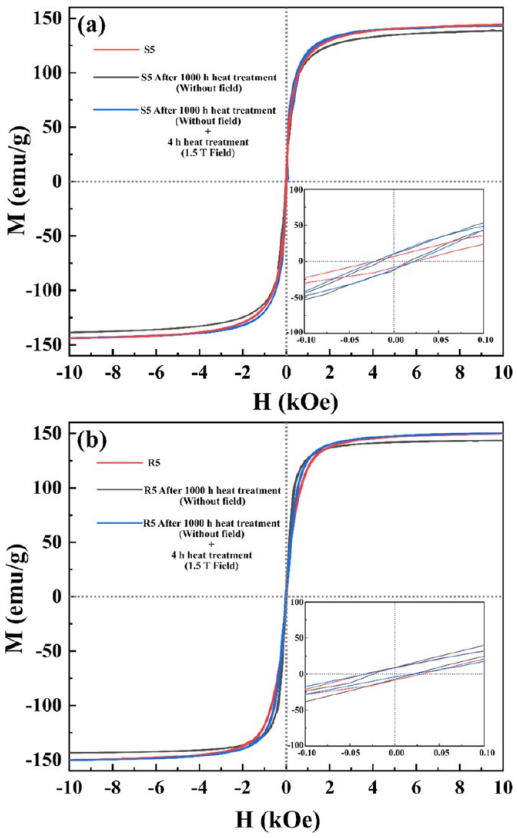

Figure 14. Comparison of M-H curves of (a) melted S5 and heat-treated S5 and (b) melted R5 and heat-treated R5.

4. CONCLUSIONS

In the current study, laser melting of 12 and 24 h mechanically milled FeNi powder was carried out successfully. It was found that the incident laser power density of 1 J/mm^2 is most suitable for producing fully dense FeNi solids from 12 to 24 h milled powders. Power density <1 J/mm^2 causes insufficient fusion of the powder particles resulting in porosity. In contrast, power density >1.4 J/mm^2 causes blowhole formation accompanied by cracks triggered due to extremely high cooling rates. The presence of a small quantity of $L1_0$ ordered FeNi has been confirmed in the laser-melted FeNi prepared from 12 h milled powder by synchrotron XRD. Laser melting of 12 h

https://doi.org/10.1021/acsomega.4c00601
ACS Omega 2024, 9, 15650−15662

milled FeNi shows larger grains (70−100 μm) with a preferred fiber texture along the <001> direction, compared to that of 24 h milled FeNi samples (15−25 μm grains), textured along the <011> direction. The difference in grain size and texture is caused due to the difference in cooling rates during solidification. Saturation magnetization is the highest (144 ± 10 emu/g) for laser-melted samples prepared at a power density of 1 J/mm^2. Coercivity and remanence are higher in the sample prepared using 24 h of milled powder than 12 h of milled FeNi powder (melted at a power density of 1 J/mm^2). The higher coercivity and remanence in the case of laser-melted samples prepared from 24 h milled powder is caused due to the smaller grains. Heat treatment near 593 K with and without an external magnetic field does not impart significant changes in the magnetic properties of the laser-melted samples.

Overall, the present study highlights the use of laser melting in production of FeNi alloy and controlling the microstructure and magnetic properties. This work lays the foundation for additive manufacturing of FeNi-based alloys with tunable magnetic properties. Future studies will be conducted highlighting the effect of laser melting of solid-shaped FeNi magnets. Also, heat treatment in the presence of a higher magnetic field will be attempted for imparting $L1_0$ ordering.

AUTHOR INFORMATION

Corresponding Author

Suddhasatwa Basu − *CSIR—Institute of Minerals and Materials Technology, Bhubaneswar 751013, India; Academy of Scientific and Innovative Research (AcSIR), Ghaziabad 201002, India; Department of Chemical Engineering, Indian Institute of Technology Delhi, New Delhi 110016, India;* orcid.org/0000-0001-7288-2370; Email: sbasu@iitd.ac.in

Authors

Shuvam Mandal − *CSIR—Institute of Minerals and Materials Technology, Bhubaneswar 751013, India; Academy of Scientific and Innovative Research (AcSIR), Ghaziabad 201002, India*

Manoj Kumar − *CSIR—Institute of Minerals and Materials Technology, Bhubaneswar 751013, India; Department of Metallurgical and Materials Engineering, Indian Institute of Technology Kharagpur, Kharagpur 721302, India*

Pradyut Sengupta − *CSIR—Institute of Minerals and Materials Technology, Bhubaneswar 751013, India; Department of Metallurgical and Materials Engineering, Indian Institute of Technology Kharagpur, Kharagpur 721302, India*

Ajit Panigrahi − *CSIR—Institute of Minerals and Materials Technology, Bhubaneswar 751013, India; Academy of Scientific and Innovative Research (AcSIR), Ghaziabad 201002, India*

Mayadhar Debata − *CSIR—Institute of Minerals and Materials Technology, Bhubaneswar 751013, India; Academy of Scientific and Innovative Research (AcSIR), Ghaziabad 201002, India*

Chandradas Shamili − *Academy of Scientific and Innovative Research (AcSIR), Ghaziabad 201002, India; Material Science and Technology Division, CSIR—Institute of Interdisciplinary Science and Technology (NIIST), Thiruvananthapuram 695019, India*

Kuzhichalil Peethambharan Surendran − *Academy of Scientific and Innovative Research (AcSIR), Ghaziabad 201002, India; Material Science and Technology Division, CSIR—Institute of Interdisciplinary Science and Technology (NIIST), Thiruvananthapuram 695019, India;* orcid.org/0000-0001-5269-1489

Indranil Manna − *Department of Metallurgical and Materials Engineering, Indian Institute of Technology Kharagpur, Kharagpur 721302, India; Birla Institute of Technology (BIT), Ranchi 835215, India*

Complete contact information is available at: https://pubs.acs.org/10.1021/acsomega.4c00601

Notes

The authors declare no competing financial interest.

ACKNOWLEDGMENTS

S.M. would like to thank Council of Scientific & Industrial Research (CSIR) for the research fellowship (31/GATE/09(14)/2018-EMR-I) and Academy of Scientific and Innovative Research (AcSIR), India, for allowing research activity through a Ph.D. program. We acknowledge Shubhra Bajpai and Santanu Pahari, CSIR-IMMT, Bhubaneswar, India, for their help during FESEM/EBSD image acquisition and analysis. G. Padma Rao, Laser lab, IIT Kharagpur is gratefully acknowledged for laser processing of FeNi samples. Dr. K. Jayasankar, CSIR-NIIST Thiruvananthpuram, India, is acknowledged for magnetic characterization. We thank Dr. Archana Sagdao for assisting in using beamline 12 at Indus-2 at RRCAT Indore, India. Special thanks to our collaborator Dr. Mukul Gupta, from UGC-DAE CSR, Indore for supporting this activity through UGC-DAE-CSR project—CRS/2021-22/01/417 (GAP-370). Prof. B. S. Murthy, IIT Hyderabad and Dr.-Ing. K. G. Pradeep, National Facility for Atom Probe Tomography (NFAPT), is acknowledged for extending the facility.

REFERENCES

(1) Chaudhary, V.; Mantri, S. A.; Ramanujan, R. V.; Banerjee, R. Additive Manufacturing of Magnetic Materials. *Prog. Mater. Sci.* **2020**, *114*, No. 100688.

(2) Goll, D.; Schuller, D.; Martinek, G.; Kunert, T.; Schurr, J.; Sinz, C.; Schubert, T.; Bernthaler, T.; Riegel, H.; Schneider, G. Additive Manufacturing of Soft Magnetic Materials and Components. *Addit. Manuf.* **2019**, *27*, 428−439.

(3) Urban, N.; Kuhl, A.; Glauche, M.; Franke, J. In *Additive Manufacturing of Neodymium-Iran-Boron Permanent Magnets*, 2018 8th International Electric Drives Production Conference, EDPC 2018-Proceedings, 2019.

(4) Schönrath, H.; Spasova, M.; Kilian, S. O.; Meckenstock, R.; Witt, G.; Sehrt, J. T.; Farle, M. Additive Manufacturing of Soft Magnetic Permalloy from Fe and Ni Powders: Control of Magnetic Anisotropy. *J. Magn. Magn. Mater.* **2019**, *478*, 274−278.

(5) Zhang, B.; Fenineche, N. E.; Liao, H.; Coddet, C. Magnetic Properties of In-Situ Synthesized FeNi3 by Selective Laser Melting Fe-80% Ni Powders. *J. Magn. Magn. Mater.* **2013**, *336*, 49−54.

(6) Dijith, K. S.; Aiswarya, R.; Praveen, M.; Pillai, S.; Surendran, K. P. Polyol Derived Ni and NiFe Alloys for Effective Shielding of Electromagnetic Interference. *Mater. Chem. Front.* **2018**, *2* (10), 1829−1841.

(7) Li, D.; Li, Y.; Pan, D.; Zhang, Z.; Choi, C. J. Prospect and Status of Iron-Based Rare-Earth-Free Permanent Magnetic Materials. *J. Magn. Magn. Mater.* **2019**, *469*, 535−544.

(8) Cui, J.; Kramer, M.; Zhou, L.; Liu, F.; Gabay, A.; Hadjipanayis, G.; Balasubramanian, B.; Sellmyer, D. Current Progress and Future Challenges in Rare-Earth-Free Permanent Magnets. *Acta Mater.* **2018**, *158*, 118−137.

https://doi.org/10.1021/acsomega.4c00601
ACS Omega 2024, 9, 15650−15662

(9) Coey, J. M. D. Perspective and Prospects for Rare Earth Permanent Magnets. *Engineering* **2020**, *6* (2), 119−131.
(10) Mandal, S.; Debata, M.; Sengupta, P.; Basu, S. L10 FeNi: A Promising Material for next Generation Permanent Magnets. *Crit. Rev. Solid State Mater. Sci.* **2022**, 1−23.
(11) Paulevé, J.; Chamberod, A.; Krebs, K.; Bourret, A. Magnetization Curves of Fe−Ni (50−50) Single Crystals Ordered by Neutron Irradiation with an Applied Magnetic Field Magnetization Curves of Fe-Ni (50−50) Single Crystals Ordered by Neutron Irradiation. *J. Appl. Phys.* **1975**, *989* (1968), 1967−1969.
(12) Sato, K.; Sharma, P.; Zhang, Y.; Takenaka, K.; Makino, A. Crystallization Induced Ordering of Hard Magnetic L10 Phase in Melt-Spun FeNi-Based Ribbons. *AIP Adv.* **2016**, *6* (5), No. 055218.
(13) Kim, J.; Kim, S.; Suh, J. Y.; Kim, Y. J.; Kim, Y. K.; Choi-Yim, H. Properties of a Rare Earth Free L1 0 -FeNi Hard Magnet Developed through Annealing of FeNiPC Amorphous Ribbons. *Curr. Appl. Phys.* **2019**, *19* (5), 599−605.
(14) Goto, S.; Kura, H.; Watanabe, E.; Hayashi, Y.; Yanagihara, H. Synthesis of Single-Phase L 10-FeNi Magnet Powder by Nitrogen Insertion and Topotactic Extraction. *Sci. Rep.* **2017**, *7*, No. 13216.
(15) Pauleve, J.; Pauthenet, R.; Laugier, J.; Dautreppe, D. Magnetic Properties of an Iron—Nickel Single Crystal Ordered by Neutron Bombardment. *J. Appl. Phys.* **1964**, *35*, 873−876.
(16) Chamberod, A.; Laugier, J.; Penisson, J. M. Electron Irradiation Effects on Iron-Nickel Invar Alloys. *J. Magn. Magn. Mater.* **1979**, *10*, 139−144.
(17) Rodríguez, V. A. P.; Rojas-ayala, C.; Medina, J. M.; Cabrera, P. P.; Quispe-marcatoma, J.; Landauro, C. V.; Tapia, J. R.; Baggio-saitovitch, E. M. Materials Characterization Fe 50 Ni 50 Synthesized by High Energy Ball Milling : A Systematic Study Using X-Ray Di Ff Raction, EXAFS and Mössbauer Methods. *Mater. Charact.* **2019**, *149*, 249−254.
(18) Montes-Arango, A. M.; Marshall, L. G.; Fortes, A. D.; Bordeaux, N. C.; Langridge, S.; Barmak, K.; Lewis, L. H. Discovery of Process-Induced Tetragonality in Equiatomic Ferromagnetic FeNi. *Acta Mater.* **2016**, *116*, 263−269.
(19) Kołodziej, M.; Śniadecki, Z.; Musiał, A.; Pierunek, N.; Ivanisenko, Y.; Muszyński, A.; Idzikowski, B. Structural Transformations and Magnetic Properties of Plastically Deformed FeNi-Based Alloys Synthesized from Meteoritic Matter. *J. Magn. Magn. Mater.* **2020**, *502*, No. 166577.
(20) Mandal, S.; Panigrahi, A.; Rath, A.; Bönisch, M.; Sengupta, P.; Debata, M.; Basu, S. Formation of L10 Ordering in FeNi by Mechanical Alloying and Field-Assisted Heat Treatment: Synchrotron XRD Studies. *ACS Omega* **2023**, *8* (15), No. 13690.
(21) Hielscher, R.; Nyyssönen, T.; Niessen, F.; Gazder, A. A. The Variant Graph Approach to Improved Parent Grain Reconstruction. *Materialia* **2022**, *22*, No. 101399.
(22) Bachmann, F.; Hielscher, R.; Schaeben, H. Texture analysis with MTEX-free and Open Source Software Toolbox. *Solid State Phenom.* **2010**, *160*, 63−68.
(23) Hielscher, R.; Schaeben, H. A Novel Pole Figure Inversion Method: Specification of the MTEX Algorithm. *J. Appl. Crystallogr.* **2008**, *41* (6), 1024−1037.
(24) Garibaldi, M.; Ashcroft, I.; Simonelli, M.; Hague, R. Metallurgy of High-Silicon Steel Parts Produced Using Selective Laser Melting. *Acta Mater.* **2016**, *110*, 207−216.
(25) Zou, J.; Gaber, Y.; Voulazeris, G.; Li, S.; Vazquez, L.; Liu, L. F.; Yao, M. Y.; Wang, Y. J.; Holynski, M.; Bongs, K.; Attallah, M. M. Controlling the Grain Orientation during Laser Powder Bed Fusion to Tailor the Magnetic Characteristics in a Ni-Fe Based Soft Magnet. *Acta Mater.* **2018**, *158*, 230−238.
(26) Carter, L. N.; Wang, X.; Read, N.; Khan, R.; Aristizabal, M.; Essa, K.; Attallah, M. M. Process Optimisation of Selective Laser Melting Using Energy Density Model for Nickel Based Superalloys. *Mater. Sci. Technol.* **2016**, *32* (7), 657−661.
(27) Simchi, A. The Role of Particle Size on the Laser Sintering of Iron Powder. *Metall. Mater. Trans. B* **2004**, *35* (5), 937−948.
(28) Zhang, J.; Gu, D.; Yang, Y.; Zhang, H.; Chen, H.; Dai, D.; Lin, K. Influence of Particle Size on Laser Absorption and Scanning Track Formation Mechanisms of Pure Tungsten Powder During Selective Laser Melting. *Engineering* **2019**, *5* (4), 736−745.
(29) Kumar, M.; Gibbons, G. J.; Das, A.; Manna, I.; Tanner, D.; Kotadia, H. R. Additive Manufacturing of Aluminium Alloy 2024 by Laser Powder Bed Fusion: Microstructural Evolution, Defects and Mechanical Properties. *Rapid Prototyp. J.* **2021**, *27* (7), 1388−1397.
(30) Kumar, M.; Das, M.; Majumdar, J. D.; Manna, I. Development of Graded Composition and Microstructure on Inconel 718 by Laser Surface Alloying with Si, Al and ZrB2 for Improvement in High Temperature Oxidation Resistance. *Surf. Coat. Technol.* **2020**, *402*, No. 126345.
(31) Hu, R.; Jin, S.; Sha, G. Application of Atom Probe Tomography in Understanding High Entropy Alloys: 3D Local Chemical Compositions in Atomic Scale Analysis. *Prog. Mater. Sci.* **2021**, *117*, No. 100740.
(32) Wheeler, J. M. Mechanical Phase Mapping of the Taza Meteorite Using Correlated High-speed Nanoindentation and EDX. *J. Mater. Res.* **2021**, *36* (1), 94−104.
(33) Carter, L. N.; Martin, C.; Withers, P. J.; Attallah, M. M. The Influence of the Laser Scan Strategy on Grain Structure and Cracking Behaviour in SLM Powder-Bed Fabricated Nickel Superalloy. *J. Alloys Compd.* **2014**, *615*, 338−347.
(34) Liu, S. Y.; Li, H. Q.; Qin, C. X.; Zong, R.; Fang, X. Y. The Effect of Energy Density on Texture and Mechanical Anisotropy in Selective Laser Melted Inconel 718. *Mater. Des* **2020**, *191*, No. 108642.
(35) Attard, B.; Cruchley, S.; Beetz, C.; Megahed, M.; Chiu, Y. L.; Attallah, M. M. Microstructural Control during Laser Powder Fusion to Create Graded Microstructure Ni-Superalloy Components. *Addit. Manuf.* **2020**, *36*, No. 101432.
(36) Sharma, P.; Zhang, Y.; Makino, A. In *Magnetic Properties of L10 FeNi Phase Developed through Annealing of an Amorphous Alloy*, 2017 IEEE International Magnetics Conference, INTERMAG 2017, 2017.
(37) Skomski, R.; Sellmyer, D. J. Intrinsic and Extrinsic Properties of Advanced Magnetic Materials. In *Handbook of Advanced Magnetic Materials*; Springer: Boston, MA, 2006; pp 1−57. DOI: 10.1007/1-4020-7984-2_1.
(38) Kołodziej, M.; Śniadecki, Z.; Musiał, A.; Pierunek, N.; Ivanisenko, Y.; Muszyński, A.; Idzikowski, B. Structural Transformations and Magnetic Properties of Plastically Deformed FeNi-Based Alloys Synthesized from Meteoritic Matter. *J. Magn. Magn. Mater.* **2020**, *502*, No. 166577.
(39) Poirier, E.; Kubic, R.; Bordeaux, N. Intrinsic Magnetic Properties of L10 FeNi Obtained from Meteorite NWA 6259. *J. Appl. Phys.* **2015**, *117*, No. 17E318.
(40) Lewis, L. H.; Mubarok, A.; Poirier, E.; Bordeaux, N.; Manchanda, P.; Kashyap, A.; Skomski, R.; Goldstein, J.; Pinkerton, F. E.; Mishra, R. K.; Kubic, R. C.; Barmak, K. Inspired by Nature: Investigating Tetrataenite for Permanent Magnet Applications. *J. Phys.: Condens. Matter* **2014**, *26* (6), No. 064213.
(41) Lima, E.; Drago, V. A New Process to Produce Ordered Fe 50 Ni 50 Tetrataenite. *Phys. Status Solidi A* **2001**, *124* (1), 119−124.
(42) Kojima, T.; Mizuguchi, M.; Takanashi, K. Growth of L10-FeNi Thin Films on Cu(001) Single Crystal Substrates Using Oxygen and Gold Surfactants. *Thin Solid Films* **2016**, *603*, 348−352.
(43) Takanashi, K.; Mizuguchi, M.; Kojima, T.; Tashiro, T. Fabrication and Characterization of L10-Ordered FeNi Thin Films. *J. Phys. D: Appl. Phys.* **2017**, *50*, No. 483002.
(44) Shima, T.; Okamura, M.; Mitani, S.; Takanashi, K. Structure and Magnetic Properties for L10-Ordered FeNi Films Prepared by Alternate Monatomic Layer Deposition. *J. Magn. Magn. Mater.* **2007**, *310* (2), 2213−2214.
(45) Mizuguchi, M.; Kojima, T.; Kotsugi, M.; Koganezawa, T.; Osaka, K.; Takanashi, K. Artificial Fabrication and Order Parameter Estimation of L10-Ordered FeNi Thin Film Grown on a AuNi Buffer Layer. *J. Magn. Soc. Jpn.* **2011**, *35*, 370−373.

https://doi.org/10.1021/acsomega.4c00601
ACS Omega 2024, 9, 15650−15662

(46) Kojima, T.; Mizuguchi, M.; Koganezawa, T.; Osaka, K.; Kotsugi, M.; Takanashi, K. Magnetic Anisotropy and Chemical Order of Artificially Synthesized L1 0-Ordered FeNi Films on Au-Cu-Ni Buffer Layers. *Jpn. J. Appl. Phys.* **2012**, *51* (1), No. 010204.
(47) Kojima, T.; Ogiwara, M.; Mizuguchi, M.; Kotsugi, M.; Koganezawa, T.; Ohtsuki, T.; Tashiro, T. Y.; Takanashi, K. Fe-Ni Composition Dependence of Magnetic Anisotropy in Artificially Fabricated L10-Ordered FeNi Films. *J. Phys.: Condens. Matter* **2014**, *26* (6), No. 064207.
(48) Tashiro, T.; Mizuguchi, M.; Kojima, T.; Koganezawa, T.; Kotsugi, M.; Ohtsuki, T.; Sato, K.; Konno, T.; Takanashi, K. Fabrication of L10-FeNi Phase by Sputtering with Rapid Thermal Annealing. *J. Alloys Compd.* **2018**, *750*, 164−170.
(49) Saito, M.; Ito, H.; Suzuki, Y.; Mizuguchi, M.; Koganezawa, T.; Miyamachi, T.; Komori, F.; Takanashi, K.; Kotsugi, M. Fabrication of L10-FeNi by Pulsed-Laser Deposition. *Appl. Phys. Lett.* **2019**, *114* (7), No. 072404.
(50) Makino, A.; Sharma, P.; Sato, K.; Takeuchi, A.; Zhang, Y.; Takenaka, K. Artificially Produced Rare-Earth Free Cosmic Magnet. *Sci. Rep.* **2015**, *5*, No. 16627.
(51) Taskaev, S. V.; Ulyanov, M. N.; Gunderov, D. V.; Bogush, M. Y. Magnetic Properties of Ternary Fe-Ni-Ti Alloys after Severe Plastic Deformation. *IEEE Magn. Lett.* **2020**, *11*, No. 2993133.
(52) Bordeaux, N.; Montes-Arango, A. M.; Liu, J.; Barmak, K.; Lewis, L. H. Thermodynamic and Kinetic Parameters of the Chemical Order-Disorder Transformation in L10 FeNi (Tetrataenite). *Acta Mater.* **2016**, *103*, 608−615.
(53) Maccari, F.; Karpenkov, D. Y.; Semenova, E.; Karpenkov, A. Y.; Radulov, I. A.; Skokov, K. P.; Gutfleisch, O. Accelerated Crystallization and Phase Formation in Fe40Ni40B20 by Electric Current Assisted Annealing Technique. *J. Alloys Compd.* **2020**, *836*, No. 155338.
(54) Maât, N.; McDonald, I.; Barua, R.; Lejeune, B.; Zhang, X.; Stephen, G. M.; Fisher, A.; Heiman, D.; Soldatov, I. V.; Schäfer, R.; Lewis, L. H. Creating, Probing and Confirming Tetragonality in Bulk FeNi Alloys. *Acta Mater.* **2020**, *196*, 776−789.

https://doi.org/10.1021/acsomega.4c00601
ACS Omega 2024, 9, 15650−15662